Neurosci Bull October 1, 2014, 30(5): 733–754. http://www.neurosci.cn
DOI: 10.1007/s12264-014-1465-9

·Review·

Recent advances in parametric neuroreceptor mapping with dynamic PET: basic concepts and graphical analyses

Seongho Seo[1,2,3], Su Jin Kim[3], Dong Soo Lee[1,3,4], Jae Sung Lee[1,2,3,5]

[1]*Department of Nuclear Medicine, College of Medicine;* [2]*Department of Brain and Cognitive Sciences, College of Natural Sciences;* [3]*Institute of Radiation Medicine, Medical Research Center;* [4]*Department of Molecular Medicine and Biopharmaceutical Sciences, Graduate School of Convergence Science and Technology;* [5]*Department of Biomedical Sciences, College of Medicine, Seoul National University, Seoul, Korea*

Corresponding author: Jae Sung Lee. E-mail: jaes@snu.ac.kr

Tracer kinetic modeling in dynamic positron emission tomography (PET) has been widely used to investigate the characteristic distribution patterns or dysfunctions of neuroreceptors in brain diseases. Its practical goal has progressed from regional data quantification to parametric mapping that produces images of kinetic-model parameters by fully exploiting the spatiotemporal information in dynamic PET data. Graphical analysis (GA) is a major parametric mapping technique that is independent on any compartmental model configuration, robust to noise, and computationally efficient. In this paper, we provide an overview of recent advances in the parametric mapping of neuroreceptor binding based on GA methods. The associated basic concepts in tracer kinetic modeling are presented, including commonly-used compartment models and major parameters of interest. Technical details of GA approaches for reversible and irreversible radioligands are described, considering both plasma input and reference tissue input models. Their statistical properties are discussed in view of parametric imaging.

Keywords: dynamic positron emission tomography; graphical analysis; neuroreceptor imaging; parametric image; tracer kinetic modeling

Introduction

Tracer kinetic modeling in dynamic positron emission tomography (PET) has played a leading role in quantitative *in vivo* studies on the functional and molecular bases of brain diseases, mainly because of its high sensitivity and quantitative accuracy[1-5]. Using a tiny amount of radioactive tracer or radioligand injected into the living body, dynamic neuroreceptor PET can accurately capture the temporally changing spatial distribution of the radioligand in the brain, which reflects the targeted receptor's density and dynamic interaction with the radioligand[6-8]. Nevertheless, the spatiotemporal distribution also contains other distracting information such as the inherent statistical noise associated with radioactive decay, and physiological factors of secondary interest[3, 7, 9]. The techniques of tracer kinetic modeling, through a mathematical framework, can refine this noisy information from PET data into several quantitative parameters that characterize the receptor distribution and/or the binding process in the brain[1, 6, 10]. Therefore, in both clinical and basic research, this method has been widely used to investigate the characteristic distribution patterns of neuroreceptors or their dysfunction, which is related to brain diseases, and the effects of new drugs[11-16].

Over the last few decades, the practical goal of tracer kinetic modeling in PET has progressed from an analysis of regional data to the production of images of kinetic-model parameters[17-19]. The typical procedure of tracer kinetic modeling involves fitting a suitable kinetic model to the tissue time-activity curves (TACs)

at the regional or voxel level that are collected from the reconstructed dynamic PET images[3, 17, 20]. The regional analysis can be easily performed at a lower computational cost and with better statistical properties owing to the smaller number and lower noise-level of the regional TACs that are usually obtained by averaging the voxel TACs within a predefined region-of-interest (ROI). However, the delineation of ROIs requires prior knowledge of the receptor distribution and is operator-dependent and time- and labor-consuming when done manually[5, 8]. More importantly, the results from regional analysis can provide only the average information within a given ROI, and their accuracy is dependent on the size of the ROI. On the contrary, the analysis of voxel TACs can fully exploit the spatiotemporal information captured in dynamic PET frames, and produce images of kinetic-model parameters that quantitatively characterize the targeted neuroreceptor system[8, 21]. Furthermore, such parametric images allow the analysis of the entire brain volume regardless of specific anatomy, such as in voxel-based statistical analysis using the SPM package (Statistical Parametric Mapping, University College London, UK)[16, 19, 22]. Therefore, the estimation of parametric images is becoming preferable, though regional analysis is still important for the exploration of the overall characteristics of tracer kinetics.

Because of the huge numbers of voxels in dynamic images and the high-level noise therein, parametric imaging is more challenging in terms of computational complexity and statistical reliability than ROI-based analysis[4, 8, 18, 19, 22]. This issue will become more crucial as the resolution of PET images improves or the injection dose of a radioligand diminishes, based on the advancement of PET scanners (e.g., high-resolution research tomography[23]). Thus, parametric imaging techniques need to be very robust to noise, computationally efficient, and moreover user-independent and automatic[17, 19].

Conceptually, most kinetic analysis techniques are applicable for the estimation of both regional parameters and parametric images. In practice, however, methods based on nonlinear parameter estimation are undesirable for parametric imaging because of a higher computational burden and less reliability than those relying on linear techniques[8, 21, 22]. Therefore, the use of compartmental analysis has long been limited mostly to regional data, although it is now being extended to voxel data thanks to the recently increased computational power and regularization techniques[24-27] developed to address the high noise-susceptibility issue. In parametric image generation, instead, preferable approaches have relied on the linearization of the standard compartment models in various ways so that computationally efficient and reliable linear estimation techniques are applicable.

One major linearization technique is to integrate the compartment model equations to produce a simple linear regression model that is linear in the parameters[17]. This method based on the simple model is called graphical analysis (GA), and its parameter estimation depends on a linear estimation technique that has a closed form solution and is thus computationally simple. In contrast to compartment modeling, in which the best model configuration needs to be determined in advance, this method achieves a level of model independence by fitting only the later portion of the measured data to a simple linear model with only two parameters[17]; this strategy enables the use of common properties among the compartmental models (steady state of specific binding). Furthermore, the results are relatively stable because they are estimated using only late time frames, which have a relatively higher signal-to-noise ratio (SNR) than earlier time frames[8]. In sum, both the simplicity of the model and the closed-form linear least squares (LLS) solution enable simple, reliable, and computationally efficient parameter estimation.

In this article, we introduce recent advances in these GA approaches, focusing on parametric image generation for neuroreceptor ligand PET studies. Although extensive applications of these approaches are based mostly on relatively fast, simple, and reliable parameter estimation rather than various other techniques, they may suffer from complicated noise structures or a limited amount of data. Hence, their statistical properties are discussed.

Basic Theory in Tracer Kinetic Modeling

Before introducing the GA methods, we briefly describe the basic concepts in tracer kinetic modeling for neuroreceptor PET studies. Throughout this paper, we follow the consensus nomenclature suggested by Innis *et al.*[28] as

much as possible. More detailed concepts and principles of tracer kinetic modeling have been presented in numerous studies[3-5, 7-9, 29-31].

Dynamic PET Acquisition

In dynamic neuroreceptor PET studies, a very small amount of radioligand with high specific activity, which is designed to follow a substrate physiological and biochemical process of interest without disturbing the associated system, is introduced into the bloodstream of an individual participant (mostly by a single intravenous bolus). The radioligand administered is delivered to capillaries in the brain by arterial blood flow, is subsequently extracted from arterial blood into tissue space across the blood-brain barrier in the capillaries, and finally binds to high-affinity receptors in the tissue through the targeted biochemical process[9]. Accordingly, the radioligand is differentially accumulated into and cleared from diverse brain tissues over time, along with the physiological and biochemical properties of the radioligand as well as the target process[8].

The characteristic spatiotemporal distribution of the radioligand in the brain can be imaged by a dynamic PET scan in which the radioactivity from the delivered radioligand is counted and then recorded in a series of image frames over irregular time intervals. Although an individual *i*th dynamic frame represents the average spatial distribution of radioactivity during the frame duration, it is usually assumed to be instantaneous at the midpoint of the frame (t_i). After a number of corrections (including a radioactivity-decay correction), reconstruction, and calibration, each dynamic PET image then represents the instantaneous measurement ($C_T^*(t_i)$) at the frame time of the time-varying radioligand concentration in each tissue region, $C_T(t)$, (Bq/mL); t is the post-injection time and the superscript * denotes noisy measurement. Therefore, by collecting the time course of the measurements from each voxel of dynamic PET images (or averaging them over the voxels within a specific ROI), we obtain voxel-wise TACs (or ROI TACs).

Compartmental Models

The measured PET data can be described with a mathematical model or a comprehensive description of the underlying processes that is developed based on a prior understanding of the kinetic behavior of radioligands in brain tissue[7-9]. Most widely used is a compartmental model that forms the basis for tracer kinetic modeling in PET[3, 29].

With prior knowledge of their expected *in vivo* kinetics, the injected radioligands can be assumed to form a limited number of separate pools, called compartments, according to their physical and chemical states. In general, the concentration of unmetabolized parent radioligand in plasma (C_P) (Bq/mL) is considered as one compartment because it serves as the input for the radioligands delivered into the tissue. As for the radioligands in the tissue, the following pools are considered plausible in studies of receptor-ligand binding: those in free form (C_F), those specifically bound to the receptor of interest (C_S), and those nonspecifically bound to other proteins (C_{NS}). Then, we have the following relationship:

$$C_T(t) = C_F(t) + C_{NS}(t) + C_S(t). \quad (1)$$

Together with several assumptions, such as homogeneous concentration and instantaneous mixing of radioligands within a compartment, the small injection dose and high specific activity enable the use of first-order rate constants to describe exchanges of radioligand between compartments[1, 2, 6, 9, 32]; so, the transport and binding rates of the radioligand are assumed to be linearly related to the concentration differences between compartments. These considerations lead to linear compartment models.

Figure 1 (top) depicts the standard two-tissue compartment model (2TCM) that involves only two compartments to represent the radioligand concentration within the tissue and that is commonly used to study neuroreceptor ligand binding. By assuming a rapid equilibrium between free and nonspecifically-bound tissue compartments, the two compartments can be considered as one unified compartment, called the non-displaceable compartment (C_{ND})[1, 2, 10]. This assumption applies well to most neuroreceptor ligand studies because of the limited temporal resolution and statistical quality of the PET data; usually, the aforementioned model containing three tissue compartments is in practice too complex to provide reliable results[3, 10]. In this model, the exchanges of radioligand are described by four rate constants: K_1 (mL/cm^3 per min) is for the delivery of the radioligand from arterial plasma to tissue while k_2 (min^{-1}) is for its efflux from tissue; and k_3 and k_4 (min^{-1}) are for the binding and release from the neuroreceptor, that is, the exchange between $C_{ND}(t)$ and $C_S(t)$.

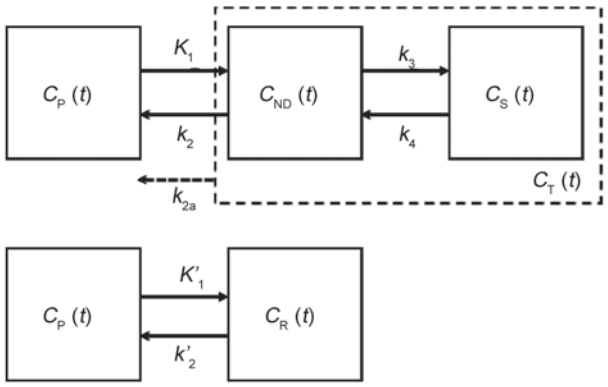

Fig. 1. Standard two-tissue compartment model for a target region or tissue (top) and one-tissue compartment model for a reference region (bottom) to describe the *in vivo* kinetic behavior of neuroreceptor radioligands. Top: concentrations (Bq/mL) of radioligands in the same states are represented as compartments: plasma concentration of unmetabolited parent radioligand (C_P), that of non-displaceable (free and nonspecifically bound) radioligand (C_{ND}), that of specifically bound radioligand (C_S); their exchanges between compartments are explained with the rate constants: K_1 (mL/cm^3 per min) and k_2–k_4 (min^{-1}); and C_T represents the total tissue concentration, that is, the sum of C_{ND} and C_S. In addition, k_{2a} denotes the apparent efflux rate constant from tissue when the tissue region can be approximately described with one compartment (dashed box) because of the equilibrium between C_{ND} and C_S. Bottom: C_R represents the total concentration in the reference region and K'_1 (mL/cm^3 per min) and k'_2 (min^{-1}) are the rate constants for their influx and efflux from C_P.

For radioligands showing fast kinetics, i.e., where the binding and release of the radioligand from the receptor are rapid enough and thereby $C_{ND}(t)$ and $C_S(t)$ are indistinguishable, the model can be further simplified into a one-tissue compartment model (1TCM)[10, 33]. In this case, the efflux rate constant k_2 is replaced by the apparent one $k_{2a} = k_2/\left(1+\frac{k_3}{k_4}\right)$. Furthermore, the 2TCM is also commonly used for irreversibly-binding radioligands whose binding process is intrinsically irreversible or seems so during the time period of PET studies. The irreversible accumulation of these radioligands can be analyzed by assuming that $k_4 = 0$.

In compartmental modeling, the final goal is to estimate the rate constants, which characterize the kinetics of the radioligand, from the measured data. Besides the measured PET data $C_T^*(t_i)$, the input function $C_P(t)$ also needs to be measured to obtain the rate constants. The process of measuring $C_P(t)$ generally relies on frequent invasive arterial blood sampling[34, 35] under the assumption that the arterial plasma concentration is the same as the capillary plasma concentration[8]; arterial blood samples are measured separately during the dynamic PET acquisition and subsequently are corrected for metabolites since the standard model assumes that no plasma metabolites cross the blood-brain barrier. As the sampling times of blood data are incompatible with dynamic frame times, some simple signal processing may be required to match them. Contrary to the measured tissue data $C_T^*(t_i)$, where t_i is the matched sampling time for the ith measurement, we also maintain $C_P(t_i)$ without the superscript for the measured input data, because the data are usually refined through plasma input modeling[36].

Although the arterial blood sampling method is considered to be the gold standard of measuring $C_P(t)$ based on its accuracy[8], it has several disadvantages such as invasiveness and technical demands[8, 31, 37]. Therefore, to minimize or eliminate the need for invasive and technically-demanding blood sampling and metabolite correction, the following approaches have been proposed and applied[37, 38]: image-derived methods[39-41], model-based methods[42-44], reference region methods[33, 45-48] and other sophisticated approaches[49-55].

In reference region methods, the kinetics of the radioligand in the tissue is described as a function of a reference region by assuming that there exists a reference area of brain tissue effectively devoid of specific binding sites[29]. Therefore, they require an additional compartment $C_R(t)$ and related rate constants K'_1 (mL/cm^3 per min) and k'_2 (min^{-1}) as shown in Figure 1 (bottom) (hereafter, the superscript ' is used for the parameters in reference tissue). As these additions increase the complexity of the model and thus uncertainty in the resulting estimates, a series of assumptions is usually made to reduce the complexity[21]: (1) nonspecific binding is the same in both areas though delivery is not, and (2) an equilibrium is rapidly achieved between C_{ND} and C_S so that tissue kinetics effectively follows the 1TCM.

Parameters of Interest in Neuroreceptor Ligand Study

In studies of reversible neuroreceptor-ligand binding, the primary outcome is the equilibrium concentration of

the radioligand specifically bound to the target receptor (C_S) that reflects the density and affinity of the receptors available to react with the radioligand *in vivo*[28]. Since the density and affinity are inseparable under the single tracer injection protocol, the concentration of specific radioligand binding is usually quantified as its equilibrium ratio to another pool of radioligand concentration, termed binding potential (BP)[6]. In the literature, there are three different practical definitions of *in vivo* BP depending on the use of distinct normalization factors (or the input measurements): non-displaceable concentration in tissue (C_{ND}), total concentration in plasma (C_P), or its free fraction ($f_P C_P$)[28]. These *in vivo* BPs represent the potential of available receptors to bind with the radioligand, and reflect the density of available receptors under the assumption that there are no substantial regional changes in receptor affinity.

For consistency throughout this article, however, we limit ourselves to $BP_{ND} = C_S(t)/C_{ND}(t)$ (unitless) because only BP_{ND} can be obtained from both the reference region model (usually directly) and from the plasma input model (indirectly) that we describe. Although the other parameters, $BP_P = C_S(t)/C_P(t)$ and $BP_F = C_S(t)/(f_P C_P(t))$, are considered to be more suitable to describe specific binding than BP_{ND}, the measurement of plasma concentration or its free fraction is necessary to estimate them. Therefore, BP_{ND} is also frequently used (in a variety of applications) mainly because of practicality. However, the interpretation of BP_{ND} requires careful attention because its use is based on the assumption that V_{ND} (more precisely, its free fraction) has no regional or group difference; the comparison of BP_{ND} may not clearly reveal the group difference associated with specific binding when V_{ND} has a group difference or treatment effect[28, 56].

Another common endpoint is the volume of distribution of total radioligand concentration in tissue (V_T). In the field of *in vivo* imaging, volume of distribution refers to the volume (mL) of plasma (with a certain concentration) required to account for the amount at equilibrium of radioligand in the unit volume (1 cm^3) of the target region, and is therefore usually represented as the ratio of the radioligand concentration in the target (tissue or compartment) to that in the plasma (mL/cm^3). Thus, V_T has the following relationship with the volume of distribution of each compartment:

$$V_T = \frac{C_T(t)}{C_P(t)} = \frac{C_{ND}(t)}{C_P(t)} + \frac{C_S(t)}{C_P(t)} = V_{ND} + V_S \quad (2)$$

where V_{ND} and V_S are the volumes of distribution for nondisplaceable and specific binding compartments, respectively.

Though V_T does not directly reflect specific binding, but rather total radioligand uptake in tissue, it is also widely used in studies of neuroreceptor binding[57]. Indeed, most GA using the plasma input function provides V_T as a major outcome. Because these methods yield a V_{ND} estimate for a receptor-free region, BP_{ND} can be indirectly computed as $BP_{ND} = V_T/V_{ND} - 1$. Similarly, even most reference region methods produce estimates of the tissue-to-reference ratio of V_T (V_T/V_{ND}), called the distribution volume ratio (DVR), to derive BP_{ND}. Furthermore, it is noteworthy that the V_S is BP_P in itself; thus, for a tracer with a high level of specific binding and/or a low level of nonspecific binding (e.g. [^{11}C] flumazenil), V_T ($\approx V_T - V_{ND} = V_S$) can yield a good estimate of the receptor density[10].

Meanwhile, the concept of BP or volume of distribution is not useful for irreversibly binding radioligands. The major outcome of interest for these radioligands is the influx rate constant (K_{in}, mL/cm^3 per min) which is the net influx rate of the radioligand from plasma into the irreversible compartment. K_{in} can be directly obtained from GA using the plasma input function, while only relative values normalized by reference region information such as K_{in}/V'_T or K_{in}/K'_{in} can be acquired from reference region methods[29].

The aforementioned parameters can be related to the rate constants of the 2TCM for reversibly binding radioligands as follows[10]:

$$V_T = \frac{K_1}{k_2}\left(1 + \frac{k_3}{k_4}\right), \quad (3)$$

$$V_{ND} = \frac{K_1}{k_2}, \quad (4)$$

$$BP_{ND} = \frac{k_3}{k_4} = \frac{V_T}{V_{ND}} - 1. \quad (5)$$

Similarly, when the 2TCM can be simplified, we can consider the following relationship:

$$V_T = \frac{K_1}{k_{2a}} = \frac{K_1}{k_2}\left(1 + \frac{k_3}{k_4}\right). \quad (6)$$

For a reference region commonly described by the 1TCM[57, 58],

we have

$$V'_{\mathrm{T}} = V'_{\mathrm{ND}} = \frac{K'_1}{k'_2}. \quad (7)$$

Therefore, under the assumption $V_{\mathrm{ND}} = \frac{K_1}{k_2} = \frac{K'_1}{k'_2} = V'_{\mathrm{ND}} = V'_{\mathrm{T}}$, reference region methods can provide direct estimation of BP by using reference region data to acquire information about the non-displaceable component in tissue. Hence, the identification of a reliable reference region effectively devoid of specific binding is crucial[56]. On the other hand, when modeling the kinetics of irreversible binding radioligands using the 2TCM with $k_4 = 0$, we have

$$K_{\mathrm{in}} = \frac{K_1 k_3}{k_2 + k_3}. \quad (8)$$

Limitations in Parametric Image Generation

Although the standard compartment model describes a linear system, it is not linear in parameters. Therefore, the estimation of parameters in compartment models requires nonlinear estimation techniques. Because of its optimal statistical accuracy and reliability[59], the NLS method is considered to be the method of choice for tracer kinetic modeling and is often used as the gold standard to assess the performance of other methods in terms of ROI parameters[8, 17]. However, nonlinear fitting approaches have no closed-form solution and are usually solved in an iterative way. This iterative approach imposes a tremendous computational burden when applied to voxel-by-voxel analysis. Furthermore, the performance of nonlinear fitting is dependent on the initial guessing of parameters; poor initial values result in finding incorrect optima at local minima of the cost function and slow convergence. In addition, an appropriate convergence threshold and constraints on the parameters should be determined by experience[5].

Graphical Analysis

The GA method is the simplest approach that relies on a linear parameter estimation technique. In some literature, the term 'graphical analysis' has been used to indicate specific early methods such as the Gjedde-Patlak (GP) plot for an irreversible system[60-62] or the Logan plot for a reversible one[57, 63]. However, it is now considered as a category rather than a specific method, since several different GA models have also been developed to measure different parameters or to improve other models[64-67]. Table 1 lists the characteristics of all GA methods.

In each GA approach, the kinetic behavior of the radioligand is described by only two variables (for a simple linear regression) that are transformed from the measured data, including input functions, and that establish a linear relationship partially and asymptotically. The slope and intercept of that asymptotic linear portion can be interpreted as physiologically meaningful parameters, such as V_{T} or K_{in}[68]. Hence, first the linearity of the relationship is examined graphically by plotting one variable *versus* the other (which is why it is called graphical analysis; see Fig. 2) and then the slope and intercept are estimated by fitting a straight line to the specified linear portion *via* the LLS method.

To model the linear portion, GA methods rely on a simple linear regression model, or a linear model with a single independent variable, of the following matrix form:

$$\mathbf{y} = \beta_1 \mathbf{x_1} + \beta_0 \mathbf{1} + \boldsymbol{\epsilon} = \mathbf{X}\boldsymbol{\beta} + \boldsymbol{\epsilon}, \quad (9)$$

where $\mathbf{y}$ and $\mathbf{x_1}$ are $n \times 1$ vectors of dependent and independent variables, respectively; $\mathbf{X} = [\mathbf{x_1}, \mathbf{1}]$ is an $n \times 2$ matrix of the $\mathbf{x_1}$ and all-ones vector ($\mathbf{1}$) for the intercept term; $\boldsymbol{\beta} = [\beta_1, \beta_0]^T$ is a vector of the 2 parameters, slope (β_1) and intercept (β_0); and $\boldsymbol{\epsilon} = [\epsilon_1, \cdots, \epsilon_n]^T$ is an $n \times 1$ vector of the error term. Then, the slope (β_1) and the intercept (β_0) characterizing the linear portion are usually obtained by solving the LLS problem:

$$\min_{\boldsymbol{\beta}} \|\mathbf{X}\boldsymbol{\beta} - \mathrm{y}\|_2^2, \quad (10)$$

which has the following closed form solution or the LLS estimator:

$$\widehat{\beta}_{\mathrm{LLS}} = (\mathrm{X}^T\mathrm{X})^{-1}\mathrm{X}^T\mathrm{y}. \quad (11)$$

The GA methods have several advantages that are mainly attained by linearizing compartment model equations into the simple linear model so that the LLS approach can be used[67, 68]. Both the simplicity of the model and the closed-form solution of the LLS method enable simple, reliable, and computationally efficient parameter estimation. Furthermore, in contrast to standard compartmental modeling, the GA methods are consistently applicable across different tissue data with no *a priori* knowledge on the best model structure for each tissue, because their equations are derived from a general multi-compartment model in which an arbitrary number of

Table 1. Overview of graphical analysis methods

	Logan plot	RE plot	GP plot	RE-GP plot	Ito plot	Noninvasive Logan	Noninvasive RE	Noninvasive GP
Binding type	Reversible	Reversible	Irreversible	Reversible	Reversible	Reversible	Reversible	Irreversible
Input function	C_P	C_P	C_P	C_P	C_P	C_R	C_R	C_R
Model equations	Eq. (12)	Eq. (18)	Eq. (24)	Eqs. (18), (24), (27) –(29)	Eq. (30)	Eq. (17)	Eq. (19)	Eq. (25)[1] (or (26))[2]
Major parameters of interest	V_T	V_T	K_{in}	V_T	V_{ND} and V_T	$V_T/V_T^{'}$	$V_T/V_T^{'}$	$K_{in}/V_T^{'}$ (or $K_{in}/K_{in}^{'}$)
Necessity of reference region or C_R	Need only to obtain BP_{ND}	Need only to obtain BP_{ND}	No	Need only to obtain BP_{ND}	No (optional for BP_{ND})	Yes	Yes	Yes (or Yes)
Model variable containing noisy data C_T^*	Both dependent & independent	None	Dependent	Dependent	Dependent	Both	Dependent	Dependent (or both)
Major effect of noise on LLS estimates	Negative bias	Variance	High variance	Variance	High variance	Negative bias	Variance	High variance (or negative bias)
Linearity condition	$\frac{C_S(t)}{C_T(t)} \rightarrow const$ (1TCM after t^*)	$\frac{C_T(t)}{C_P(t)} \rightarrow const$	$\frac{C_{ND}(t)}{C_P(t)} \rightarrow const$	$\frac{C_S(t)}{C_T(t)} \rightarrow const$ (1TCM after t^*)	$\frac{C_S(t)}{C_T(t)} \rightarrow const$ (1TCM after t^*)	Logan condition for tissue and reference	RE condition for tissue and reference	Logan for reversible and GP for irreversible
Reference	Logan *et al.* (1990)[63]	Zhou *et al.* (2009)[66]	Gjedde (1981)[60] and Patlak *et al.* (1983)[61]	Zhou *et al.* (2010)[67]	Yokoi *et al.* (1993)[64] and Ito *et al.*, (2010)[65]	Logan *et al.* (1996)[57]	Zhou *et al.* (2009)[66]	Patlak and Blasberg (1985)[62], Wu (2008)[37], and Zheng *et al.* (2012)[38]

[1]Model for reference region with reversible kinetics. [2]Model for reference region with irreversible kinetics (note that this is not a typical graphical analysis). BP_{ND}, *in vivo* binding potential given as the ratio at equilibrium of specifically bound radioligand to that of non-displaceable radioligand in tissue; C_{ND} (or C_S), concentration of non-displaceable (or nonspecifically bound) radioligand in tissue; C_P, plasma concentration of unmetabolized parent radioligand; C_R, total concentration in reference region; C_T^*, measure PET data (total concentration in tissue); GP, Gjedde-Patlak; K_{in}, net influx rate of the radioligand from plasma into the irreversible compartment; LLS, linear least squares; RE, relative equilibrium; V_T (or V_{ND}), volume of distribution of total tissue (or non-displaceable) radioligand concentration (superscript prime means that the parameter is associated with reference region).

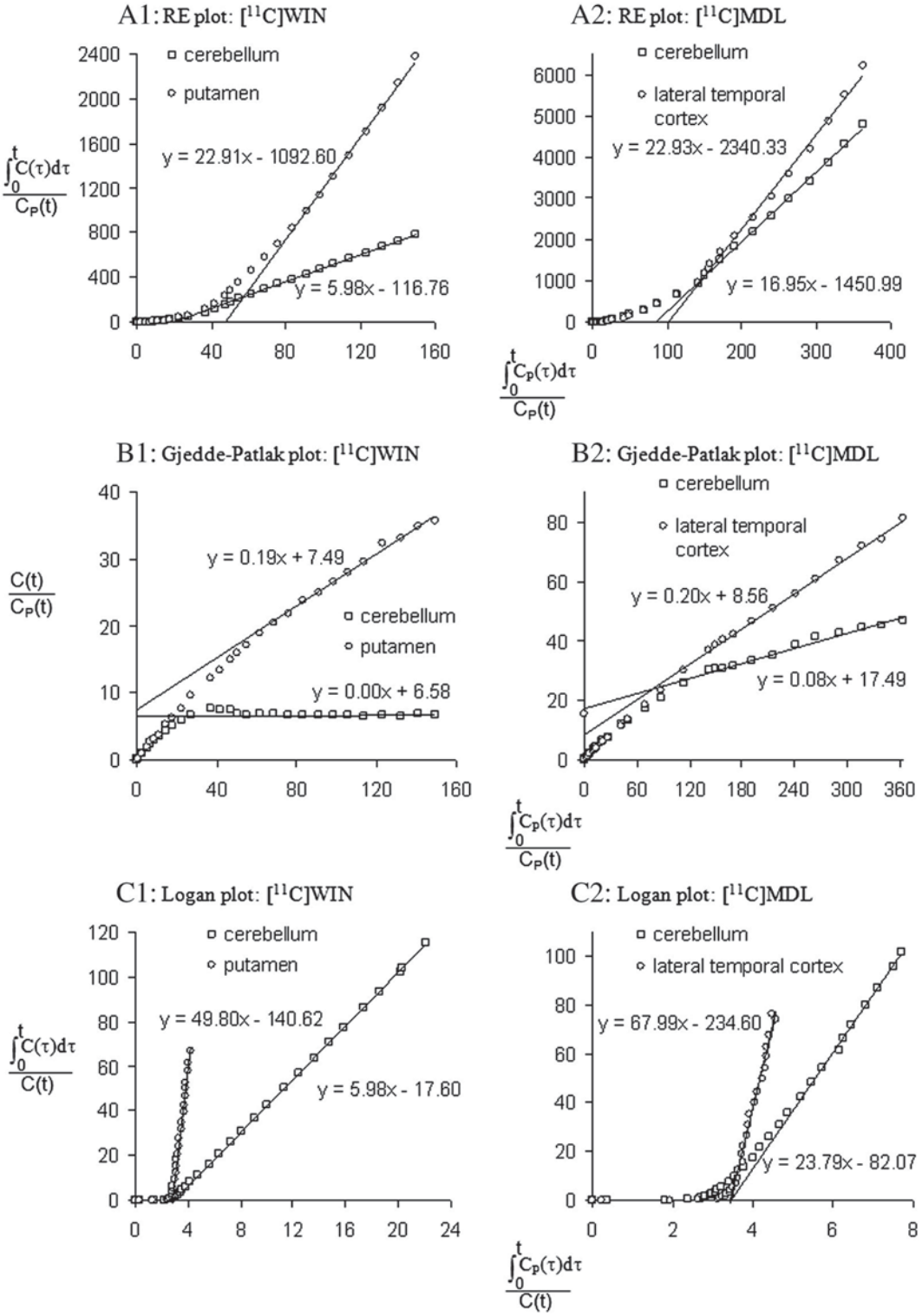

Fig. 2. Various graphical plots for the slow kinetic radiotracers, [^{11}C]WIN (left) and [^{11}C]MDL (right). (A) Relative equilibrium (RE), (B) Gjedde-Patlak, and (C) Logan plots (reprinted from Zhou *et al.* Neuroimage 2010[67] with permission).

compartments is assumed[61, 63]. These strengths of GA methods can greatly facilitate the generation of parametric images in which numerous voxels covering various brain regions can be analyzed.

However, a series of assumptions underlie the linearization and simplification of kinetic models for GA that allows the use of simple linear regression and thus provides various advantages. First, GA methods require the determination of t^*, the time when the plot becomes linear, because the model is valid only for the later part of the dynamic frames. A poor determination can yield erroneous estimates by violating the linearity requirement. In addition, slow kinetic tracers have a late starting point of the linear portion that reduces the amount of data available for estimation. Thus, the results can suffer from high uncertainty because of limited data. Moreover, unbiased parameter estimation in the simple linear regression depends on basic assumptions of LLS: that there are no or negligible errors in the independent variable of the linear model, and that the independent variables are uncorrelated with the error term. Any violation of these conditions can lead to inaccurate results.

Because most PET radioligands bind reversibly, reversible radioligand models have been used extensively[1, 69]. Therefore, though most of them were extended from the GP plot for an irreversibly binding radioligand (the first GA method), we introduce the reversible radioligand models first.

Reversible Radioligand Models

Logan plot The Logan plot (Fig. 2) is a representative graphical method used to analyze a reversible radioligand-receptor binding[57, 63]. The model equation using the plasma input function is given by

$$\frac{\int_0^t C_{\mathrm{T}}(s)ds}{C_{\mathrm{T}}(t)} = V_{\mathrm{T,Logan}}\frac{\int_0^t C_{\mathrm{P}}(s)ds}{C_{\mathrm{T}}(t)} + \beta_{\mathrm{Logan}} \text{ for } t > t^*, \quad (12)$$

where $V_{\mathrm{T,Logan}}$ is the total distribution volume, and t^* is the time when the intercept β_{Logan} becomes effectively constant. Given the measured noisy TAC, $C_{\mathrm{T}}^*(t_i)$ $(1 \le i \le n)$ obtained from n sequential dynamic frames, we have

$$y_i = \int_0^{t_i} C_{\mathrm{T}}^*(s)ds / C_{\mathrm{T}}^*(t_i),\ x_{1i} = \int_0^{t_i} C_{\mathrm{P}}(s)ds / C_{\mathrm{T}}^*(t_i),$$

and $\boldsymbol{\beta} = [V_{\mathrm{T,Logan}}, \beta_{\mathrm{Logan}}]^T$ for $1 \le i \le n$. y_i and x_{1i} are the ith elements of $\mathbf{y}$ and $\mathbf{x_1}$, respectively. Here, $\int_0^{t_i} C_{\mathrm{T}}^*(s)ds$ represents the numerical integration of $C_{\mathrm{T}}^*(t_i)$ that are discrete sample data, not the integral of a continuous function.

As in other GA methods, the Logan plot is consistently applicable to data from different voxels or ROIs regardless of their underlying model configurations. However, if a particular model configuration is assumed for the given data, $V_{\mathrm{T,Logan}}$ and β_{Logan} can be related to the specific rate constants included in that configuration; usually the 1TCM or the 2TCM is considered for receptor-ligand studies. The slopes are differently interpreted as Equations (3) or (7), according to the model configurations. For the 1TCM (without k_3 and k_4), the linearity is simply met for all the frame times since $\beta_{\mathrm{Logan}} = -1/k_2$. On the contrary, for the 2TCM, we have to determine t^* because the intercept is not actually a constant:

$$\beta_{\mathrm{Logan}} = -\frac{1}{k_2}\left(1 + \frac{k_3}{k_4}\right) - \frac{1}{k_4}\frac{C_S(t)}{C_T(t)}. \quad (13)$$

The limit value $-1/k_{2a}^*$ is defined at the steady-state condition of tissue tracer kinetics $\left(\frac{dC_{\mathrm{ND}}(t)}{\mathrm{d}t} = 0\ \&\ \frac{dC_S(t)}{\mathrm{d}t} = 0\right)$:

$$\beta_{\mathrm{Logan}} \to -\frac{1}{k_2}\left(1 + \frac{k_3}{k_4}\right) - \frac{1}{k_4}\frac{k_3}{k_3 + k_4} = -\frac{1}{k_{2a}^*}. \quad (14)$$

However, the constancy of β_{Logan} can be approximately achieved before the steady state, yielding a good estimate of $V_{\mathrm{T,Logan}}$[63, 68, 70].

Meanwhile, the Logan equation can be re-written for a reference region:

$$\frac{\int_0^t C_{\mathrm{R}}(s)ds}{C_{\mathrm{R}}(t)} = V'_{\mathrm{T,Logan}}\frac{\int_0^t C_{\mathrm{P}}(s)ds}{C_{\mathrm{R}}(t)} + \beta'_{\mathrm{Logan}} \text{ for } t > t^*. \quad (15)$$

Rearranging Equation (15) gives

$$\int_0^t C_{\mathrm{P}}(s)ds = \frac{1}{V'_{\mathrm{T,Logan}}}\left(\int_0^t C_{\mathrm{R}}(s)ds - \beta'_{\mathrm{Logan}}C_{\mathrm{R}}(t)\right). \quad (16)$$

Then, by approximating the plasma integral in Equation (12) using Equation (16), the noninvasive Logan plot based on a reference TAC can be obtained as follows:

$$\frac{\int_0^t C_{\mathrm{T}}(s)ds}{C_{\mathrm{T}}(t)} = \frac{V_{\mathrm{T,Logan}}}{V'_{\mathrm{T,Logan}}}\left(\frac{\int_0^t C_{\mathrm{R}}(s)ds - \beta'_{\mathrm{Logan}}C_{\mathrm{R}}(t)}{C_{\mathrm{T}}(t)}\right) + \beta_{\mathrm{Logan}}. \quad (17)$$

If the reference region is approximately devoid of receptor sites, BP_{ND} can be determined as $V_{\mathrm{T,Logan}}/V'_{\mathrm{T,Logan}} - 1$ under the assumption that $\frac{K_1}{k_2} = \frac{K_1'}{k_2'}$.

There are several tips for technical efficiency in the implementation of the noninvasive Logan plot. The slope in Equation (17), the DVR, may be stably

estimated by using a population average of $\beta'_{\text{Logan}}, \bar{\beta}'_{\text{Logan}}$, (or the more physiologically meaningful $\bar{k}'_2$) in place of the individual β'_{Logan} (or k'_2). In this case, the inter-subject variability in β'_{Logan} is blended into an error term of the model and then removed by the fitting process. In addition, the term $\frac{\beta'_{\text{Logan}} C_{\text{R}}(t)}{C_{\text{T}}(t)}$ can be ignored when it is relatively small or becomes constant[57]; in fact, the term is merged into the error or the intercept term. It is noteworthy that, although the term in parenthesis in Equation (17) is treated as one independent variable in the noninvasive Logan plot method, it can be used as two separate variables for the parameter estimation[71] that requires multiple linear regression analysis.

Because of its diverse merits, such as model independence, computational efficiency, simple implementation, and statistical reliability under low-noise data, the Logan plot has been extensively used in neuroreceptor binding studies. However, the Logan plot suffers from a crucial limitation, especially in parametric imaging (Figs. 3 and 4), in that it produces a severe negative bias in $V_{\text{T,Logan}}$ or $\frac{V_{\text{T,Logan}}}{V'_{\text{T,Logan}}}$ when $C_{\text{T}}(t)$ is highly contaminated[72-74]. As shown in Equations (12) and (17), the noise in $C_{\text{T}}(t)$ is entered into both the independent and dependent variables of its model equation while establishing a correlation between them, which therefore makes the model violate the LLS assumptions mentioned. Furthermore, the magnitude of the bias depends on the noise level that is also dependent (but not linearly) on the radioactivity concentration[72-75]. The effect of noise is also not consistent throughout the parametric image space; high-binding regions usually undergo more severe underestimation. One minor disadvantage of the Logan plot is the requirement of full dynamic scanning to compute $\int_0^t C_{\text{T}}(s)ds$, though only the later parts of the measurements (after t^*) are used for parameter estimation.

Relative equilibrium plot To address the noise-dependent bias issue in the Logan plot, the relative equilibrium-based graphical method (RE plot) was developed for both plasma and reference tissue input functions[66]. When the tissue to plasma concentration ratio, $\frac{C_{\text{T}}(t)}{C_{\text{P}}(t)}$, becomes a constant, i.e., the RE established after a certain time t^* (Fig. 5, left), tracer concentrations satisfy the following relationship:

$$\frac{\int_0^t C_{\text{T}}(s)ds}{C_{\text{P}}(t)} = V_{\text{T,RE}} \frac{\int_0^t C_{\text{P}}(s)ds}{C_{\text{P}}(t)} + \beta_{\text{RE}} \text{ for } t > t^*. \quad (18)$$

This model can be derived from compartment model equations or by multiplying the Logan plot model (Equation (12)) by $\frac{C_{\text{T}}(t)}{C_{\text{P}}(t)}$. Note that the constant ratio of tissue-to-plasma concentrations can be achieved at the steady state, but it is also possible to achieve it earlier than the steady state. However, this generally requires somewhat longer times than the Logan linearity condition $(\frac{C_{\text{S}}(t)}{C_{\text{T}}(t)} \rightarrow const)$[68].

In addition, when a reference region is also in the RE state for $t > t^*$ $(\frac{C_{\text{R}}(t)}{C_{\text{P}}(t)} = r)$, we have the noninvasive RE plot model as follows:

$$\frac{\int_0^t C_{\text{T}}(s)ds}{C_{\text{R}}(t)} = \frac{V_{\text{T,RE}}}{V'_{\text{T,RE}}} \frac{\int_0^t C_{\text{R}}(s)ds}{C_{\text{R}}(t)} + \frac{1}{r}\left(\beta_{\text{RE}} - \frac{V_{\text{T,RE}}}{V'_{\text{T,RE}}}\beta'_{\text{RE}}\right), \quad (19)$$

where $V'_{\text{T,RE}}$ and β'_{RE} are the slope and intercept of the RE plot in the reference region. Thus, the invasive RE plot can provide BP_{ND} if the non-receptor region is used for the reference region.

One merit of the RE plot is its high computational efficiency. As shown in Equations (18) and (19), the independent variable is not dependent on the tissue data and is common over all voxel TACs. Therefore, once **X** $(x_{1i} = \int_0^{t_i} C_{\text{P}}(s)ds / C_{\text{P}}(t_i)$ or $\int_0^{t_i} C^*_{\text{R}}(s)ds / C^*_{\text{R}}(t_i))$ is computed from the input function, it can be used for all tissue data, that is, only one matrix conversion is required for parametric image generation. However, in the case of the Logan plot, **X** needs to be computed and inverted for every voxel. In addition, it is noteworthy that both independent and dependent variables in Equations (18) and (19) have a much lower noise level compared with $C^*_{\text{T}}(t)$ because the integration reduces fluctuations in the later part of TAC, and $C_{\text{R}}(t)$ is obtained by averaging voxel TACs over a reference ROI. Therefore, the RE plot can achieve effectively unbiased estimation with low variance provided that linearity is established. However, for linearity, tissue tracer kinetics must be at a relative equilibrium state during PET scans, and thus only late data points can be used for the estimation. Thus, good precision properties obtained from a less noisy dependent variable could be

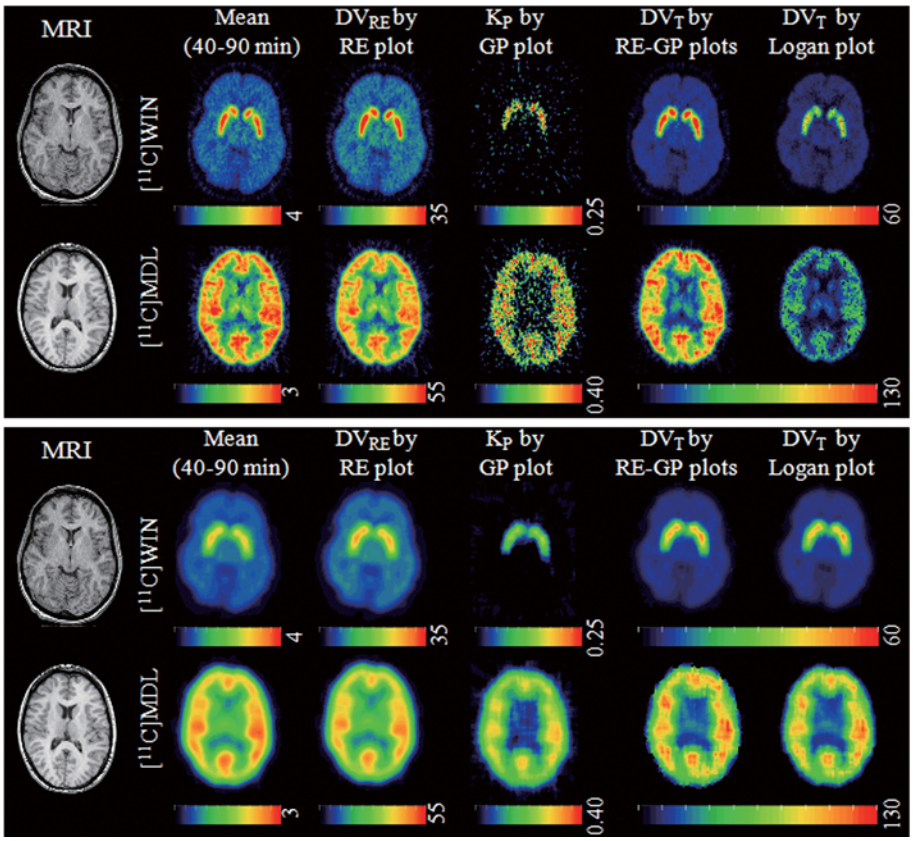

Fig. 3. Top: parametric images of V_T (represented as DV_{RE} or DV_T) and K_{in} (represented as K_P) from various methods: RE plot, RE-GP plot, and Logan plot (reprinted from Zhou *et al.* Neuroimage 2010[67] with permission). Bottom: results from de-noised dynamic images (reprinted from Zhou *et al.* Neuroimage 2010[67] with permission).

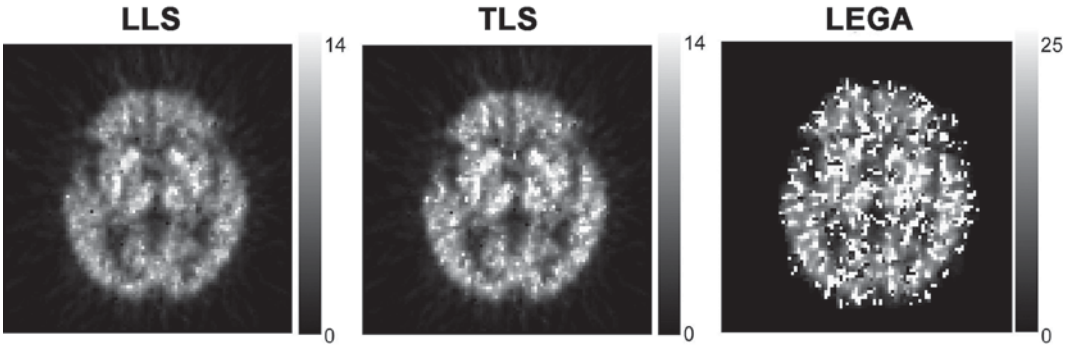

Fig. 4. V_T images from the Logan plot with linear least squares (LLS), total least squares (TLS), and likelihood estimation in graphical analysis (LEGA). The images were made from the same original PET data using [^{11}C]SA4503, a radioligand for the σ_1 receptor (reprinted from Kimura *et al.* Ann Nucl Med 2007[75] with permission).

compromised with the data reduction because of the relatively late t^*.

Bias reduction for Logan plot In addition to the RE plot, there have been a variety of attempts to reduce the bias in the LLS estimates from the Logan plot[19, 36, 56, 69, 76-80]. Those approaches can be categorized by (1) methods to increase the SNR in dynamic images, and (2) those that adopt more sophisticated estimation techniques. In this subsection, we

introduce these two categories.

Data de-noising The most simple and straightforward solution to the bias issue in the Logan plot may be to apply smoothing techniques directly to the dynamic data. Although smoothing approaches are effective, they are not a direct improvement over the Logan plot[81] and thus can be applied not only to GA but also to all other methods that are affected by noise in the dynamic data. Logan *et al.*[76] used generalized linear least squares (GLLS)[42, 82] as a temporal smoothing technique to reduce noise in TAC data, and subsequently applied the Logan plot to the noise-reduced TACs, the result of GLLS. This combination of the Logan plot and GLLS yielded unbiased estimates of V_T up to intermediate noise levels, but suffered from overestimation and significant variability at high noise levels. Joshi *et al.*[79] suggested the use of principal component analysis (PCA) for the temporal smoothing of TACs. This PCA-based approach demonstrated good performance with both increased accuracy and precision. However, it requires pre-processing for the selection of optimal principal components, and too many components may reintroduce a bias. For spatial domain de-noising, grouping TACs with similar properties such as proximity or functional relations may also be useful[68, 77, 83]. The main drawback of spatial smoothing techniques is a loss of spatial resolution and additional partial volume effects (Fig. 3 bottom)[67]. Cselényi *et al.*[19, 80] proposed two wavelet-based de-noising techniques that can overcome the noise susceptibility with generally good accuracy and not much loss of spatial resolution. However, these techniques are computationally demanding compared with other approaches. In addition to these methods, many other approaches aimed at increasing the SNR of the reconstructed images are also applicable[27].

Total least squares (TLS) Varga and Szabo[78] proposed the use of TLS estimation[84], also referred to as the 'perpendicular linear regression model', instead of LLS for the Logan plot model because the TLS considers the noise in the independent as well as in the dependent variables. The TLS method seeks to minimize the following sum of squared orthogonal distances from the measured points to the fitted line (or hyperplane), by perturbing all the noisy variables **X** and **y**, as follows:

$$\min_{\boldsymbol{\beta}=[\beta_1,\beta_0]^T} \frac{\|\mathbf{X}\boldsymbol{\beta}-\mathbf{y}\|_2^2}{1+\beta_1^2}. \quad (20)$$

Although this approach may seem to be complicated, it has a closed form solution and thus maintains computational simplicity like LLS.

In the original work[78], using this TLS method showed that the bias was dramatically reduced and thus the resulting V_T was consistent in accuracy regardless of the noise levels of the TAC but at the expense of increasing variance (Fig. 4). However, such good performance was not reproduced well in other studies where the TLS only partially removed bias[19, 68, 75, 85]. Although the reason for such discrepancy in the performance between studies is unclear, there are some speculated sources for the remaining bias: a heterogeneity of variances or a correlation between the noise in all the variables[84, 85]. We speculate that the poor performance of TLS in the Logan plot is mainly due to high noise correlation because the same noise is shared in all the variables of the Logan model through the denominator ($C_T^*(t)$).

Likelihood estimation in graphical analysis (LEGA) Ogden[36] proposed the LEGA method to suppress the noise-induced bias in the result of the Logan plot. However, the LEGA method implicitly uses the Logan model, unlike other bias-reduction approaches that transform the measured TAC and then directly use the Logan model equation[19, 69, 76-80]; the Logan model is converted into the following recurrence relation to generate the noise-free TAC predicted by the model,

$$C_T(t_i)=\frac{\sum_{j=1}^{i-1}\Delta t_j C_T(t_j)+\frac{1}{8}\Delta t_i C_T(t_{i-1})-V_{T,Logan}\int_0^{t_i}C_P(s)ds}{\beta_{Logan}-\frac{3}{8}\Delta t_i}, \quad (21)$$

for $k \le i \le n$, where Δt_i denotes the duration of the ith frame, $C_T(t_i)$ is the predicted tissue concentration at the mid-frame time t_i (for $k \le i \le n$), and k is the index of the first frame satisfying $t_i > t^*$. Then, the solution of the following least squares problem,

$$\min_{V_{T,Logan}\ \&\ \beta_{Logan}} \left\{\sum_{i=k}^{n} C_T^*(t_i)-C_T(t_i)\right\}^2, \quad (22)$$

provides maximum likelihood estimators for $V_{T,Logan}$ and β_{Logan} under the assumption that errors in the values of the measured TAC, $C_T^*(t_i)$, are independently and identically distributed normal random variables with zero mean. Because Equation (21) is valid only for $k \le i \le n$, the measured values of $C_T^*(t_i)$ for $1 \le i \le k-1$ are used for the calculation of $C_T(t_k)$. The LEGA that was originally

developed for the plasma input function was also extended to a reference region method with more complicated update equations for both target tissue and reference tissue TACs[56].

Since the LEGA method applies the likelihood estimation not to the transformed data but to the original TAC ($C_T^*(t_i)$), it can circumvent the bias issue associated with the Logan model. However, it does not provide any graphical inspection of the binding characteristic, in contrast to the Logan plot. Hence, to choose a proper value of t^* or k, it needs to rely on the Logan plot or other t^*-selection approaches[85]. Furthermore, because of the recurrence of predicted values and the nonlinear involvement of $V_{T,Logan}$ and β_{Logan}, the solution must be computed using an iterative nonlinear optimization algorithm (at least over one-dimensional parameter space for β_{Logan}); the results of the Logan plot may be used for the initial values for the iteration, and for surrogate values when numerical instability occurs.

The major drawback of LEGA in parametric imaging is that the improved accuracy is accomplished at the expense of precision loss that contributes to noisy parametric images as shown in Figure 4[81, 86]. To improve the variance properties of LEGA, Shidahara *et al.*[81] suggested a new method based on a maximum *a posteriori* estimation, where a physiological range of parameters is incorporated as prior knowledge and the measured TAC is compared with the predicted TAC, not in the original TAC space, but in the lower-dimensional space that is reduced from the original space using PCA.

Instrumental variable (IV) Logan *et al.*[69] introduced the IV method[87, 88] to address the bias problem encountered in the Logan plot because of the noise in the independent variable. In several disciplines including statistics, the IV method is basically used to remove a correlation between the independent variables ($\mathbf{X}$) and the error term ($\boldsymbol{\epsilon}$) that can lead to biased estimates in standard linear regression. Although the correlation between $\mathbf{X}$ and $\boldsymbol{\epsilon}$ can stem from the noise in the independent variable (even if it is uncorrelated with the noise in the dependent variable) as well as several other sources, the IV method can eliminate the bias regardless of its source[89]. In addition, TLS can also be considered as a variation on the IV method with a specific instrument that is nonetheless not used explicitly; however, the IV method makes no assumptions about the noise models, unlike the TLS[90].

The key concept in the IV method is the use of one or more extra variables (not in the model), called instrumental variables or instruments, to separate the (exogenous) part of $\mathbf{X}$ that is uncorrelated with $\boldsymbol{\epsilon}$ from the remaining (endogenous) part that is correlated with $\boldsymbol{\epsilon}$. Only the segregated exogenous part of $\mathbf{X}$ is then used for the parameter estimation because the endogenous part is the source of bias in the LLS estimates; given the instruments $\mathbf{Z}$, the IV estimator is defined as

$$\hat{\beta}_{IV} = (\mathrm{Z}^T\mathrm{X})^{-1}\mathrm{Z}^T\mathrm{y} \quad (23)$$

This estimator yields unbiased estimates if $\mathbf{Z}$ is uncorrelated with $\boldsymbol{\epsilon}$, and if it is correlated with the endogenous independent variables after removing the effect on them of the other uncorrelated exogenous variables (i.e., conditional on the other independent variables).

The critical point of the IV method is to construct legitimate instruments satisfying these requirements. Logan *et al.*[69] suggested two methods for the construction: an

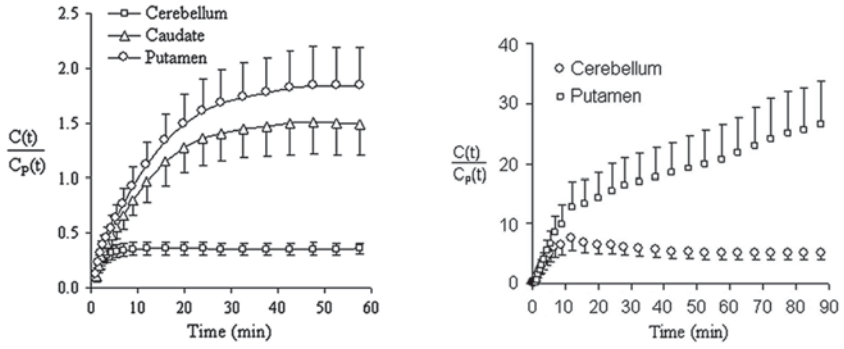

Fig. 5. Left: relative equilibrium (RE) state after t^* = 42.5 min in [^{11}C]raclopride PET (reprinted from Zhou *et al.* Neuroimage 2009[66] with permission). Right: violation of RE condition in [^{11}C]WIN PET (reprinted from Zhou *et al.* Neuroimage 2010[67] with permission).

iterative approach proposed by Minchin[91] and another based on less noisy regional TACs. The main idea common to the two methods is to use $Z = [\int_0^{t_i} C_P(s)ds / C_T(t_i), 1]$, the denoised version of **X** that can be considered as the exogenous part of **X** by itself when the correlation between **X** and ϵ is primarily due to the noise in **X**. The first method involves the prediction of $C_T(t_i)$ using Equation (21) and the parameter estimates from the original Logan plot, and the subsequent computation of $\hat{\beta}_{IV}$; this process is repeated until $\hat{\beta}_{IV}$ converges. In the second method, a regional TAC of a large ROI is used for $C_T(t_i)$, and $\hat{\beta}_{IV}$ is estimated without any iteration. Because the iterative approach has convergence issues, the second method is preferable. Furthermore, according to Logan *et al.*[69], the second method showed good results when the smoothed reference TAC was used in **Z**. On the other hand, the IV approach was extended to the noninvasive Logan plot but **Z** was constructed using only the second method based on ROI TACs.

The IV methods successfully reduce the bias but at the expense of variance, much as in other bias-reduction approaches. Instead of improving the IV method itself, to reduce both the bias and variability, Logan *et al.*[69] suggested the use of the median of the values determined by various modifications of the Logan plot as well as the IV method, methods that have different noise characteristics for the same data.

Irreversible Tracer Models

Invasive Gjedde-Patlak (GP) plot methods For a tracer with an irreversible binding, the GP plot[60-62] (Fig. 2) has been widely used. Although the term 'Patlak plot' or simply 'graphical analysis' is often used for this method, we keep the 'GP plot' for consistency with the RE-GP plot throughout the paper.

The model equation including the plasma input function (Equation (24)) can be obtained from the 2TCM by assuming k_4 = 0 as well as from a general multi-compartment model[61, 63]. When an equilibrium has been established between the plasma and reversible components (or $\frac{C_{ND}(t)}{C_P(t)}$ becomes effectively constant) for $t > t^*$, the following linear model achieves an asymptotic linearity for an irreversibly-binding tracer:

$$\frac{C_T(t)}{C_P(t)} = K_{in,GP}\frac{\int_0^t C_P(s)ds}{C_P(t)} + \beta_{GP} \text{ for } t > t^*, \quad (24)$$

where the influx rate constant $K_{in,GP} = \frac{K_1 k_3}{k_2 + k_3}$ and the intercept term $\beta_{GP} = \frac{k_2}{k_2+k_3}\frac{C_{ND}(t)}{C_P(t)}$. Thus, β_{GP} has a positive value in contrast to its equivalents in the Logan or RE plots.

In addition to the common advantages of GA methods, the GP plot has a discriminative one in that it does not require a full dynamic scan because the integration of $C_T(t)$ is not involved, in contrast to other methods such as the Logan plot or the RE plot. Furthermore, it is noteworthy that the GP plot has a model equation very similar to the RE plot (Equation (18)), except for how $C_T(t)$ is involved in a dependent variable. Therefore, the two methods share similar bias properties and computational efficiency owing to using the same independent variable. On the other hand, the variance of the parameter estimate from the GP plot is more sensitive to noise (Fig. 6) than that from the RE plot because $C_T(t)$ (i.e., more noisy data) is directly involved in the dependent variable of the GP plot, while its integration (i.e., less noisy data) is used in the RE plot. This noise sensitivity of the GP plot can be improved through multiple linear analysis for irreversible radiotracers (MLAIR) methods[22]. Moreover, for a tracer assumed to have effectively irreversible binding ($k_4 \approx 0$) over the scan duration, $K_{in,GP}$ may be underestimated if the dissociation of binding is appreciable[8]; in such a case, a more general model equation is required to obtain unbiased results[62].

Noninvasive GP plot methods Concerning the reference region model, the GP plot has two different model equations according to the tracer's binding type in the reference region. When the reference region has only reversible binding sites, the relationship between $C_P(t)$ and $C_R(t)$ can be represented by the Logan plot equation with a slope $V'_{T,Logan}$ and an intercept β'_{Logan} (for $t > t^*$). Then, by multiplying both sides of Equation (24) by $\frac{C_P(t)}{C_R(t)}$ and substituting Equation (16) into Equation (24), a noninvasive GP plot model can be obtained as follows:

$$\frac{C_T(t)}{C_R(t)} = \frac{K_{in,GP}}{V'_{T.Logan}}\frac{\int_0^t C_R(s)ds}{C_R(t)} + \left\{\frac{C_P(t)}{C_R(t)}\beta_{GP} - \frac{K_{in,GP}}{V'_{T.Logan}}\beta'_{Logan}\right\}. \quad (25)$$

Thus, the slope and the intercept terms can be estimated using simple linear regression when $\frac{C_P(t)}{C_R(t)}\beta_{GP}$ $(\propto \frac{C_{ND}(t)}{C_R(t)})$ and β'_{Logan} become effectively constant for $t > t^*$[62, 68]. Meanwhile, for a reference region with irreversible uptake, the invasive GP equation is used to describe $C_P(t)$ using

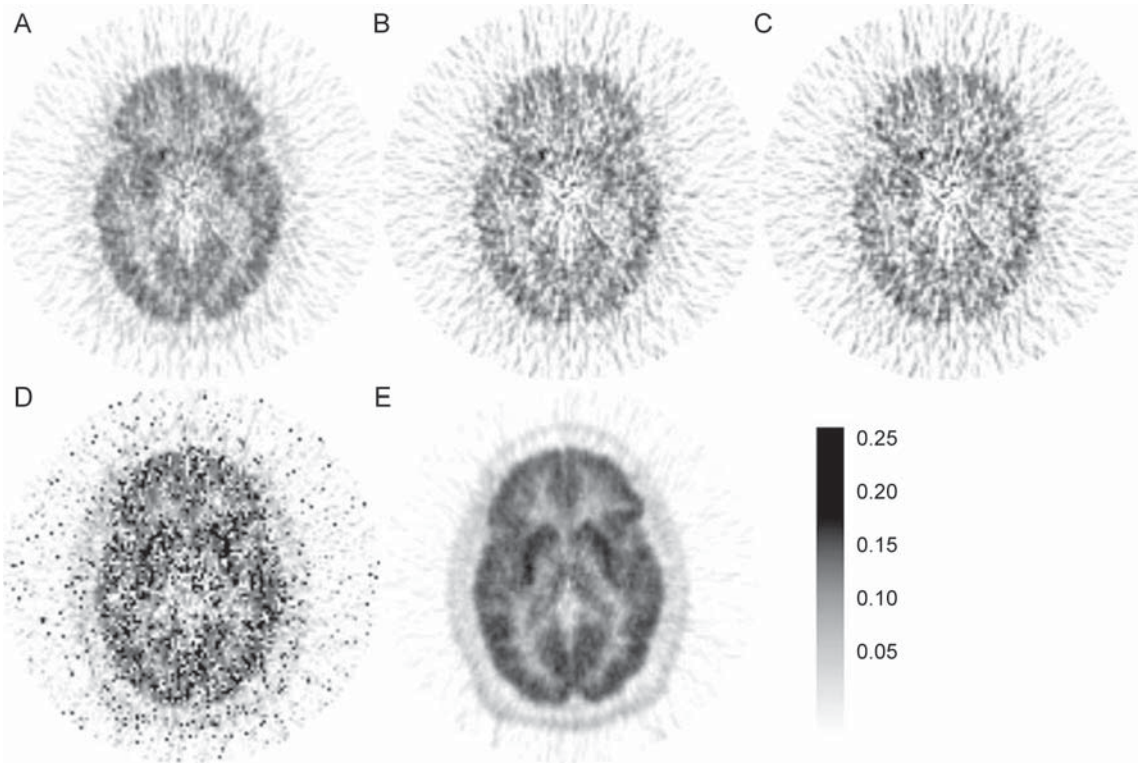

Fig. 6. K_{in} parametric images from 90-min [^{11}C]MeNTI PET of a healthy volunteer obtained using various methods: (A) GP plot using t^* = 10 min, (B) GP plot using t^* = 20 min, (C) GP plot using t^* = 30 min, (D) MLAIR1, and (E) MLAIR2 (reprinted from Kim *et al.* J Cereb Blood Flow Metab 2008[22] with permission; GP: Gjedde-Paltak, MLAIR: multiple linear analysis for irreversible radiotracers).

$C_R(t)$. Then, another linear model of a noninvasive GP plot can be obtained as follows[37, 38],

$$\int_{t^*}^{t} C_T(s)ds = \frac{K_{in,GP}}{K'_{in,GP}}\int_{t^*}^{t} C_R(s)ds + \frac{\beta_{GP}}{K'_{in,GP}}[C_R(t) - C_R(t^*)] - \frac{\beta'_{GP}}{K'_{in,GP}}[C_T(t) - C_T(t^*)] \text{ for } t > t^*, \quad (26)$$

where $K'_{in,GP}$ and β'_{GP} are the slope and intercept of the invasive GP plot applied to the reference region. This method requires that the kinetics of the radioligand in both the tissue and reference regions can be modeled using the invasive GP plot (Equation (24)).

The former noninvasive model would inherit all the properties of the original invasive GP plot model, provided that a sufficiently large ROI size is used so as to obtain $C_R(t)$ with as low a noise-level as that of $C_P(t)$; otherwise, the accuracy of the resulting estimates can be damaged by the noisy independent variable, like in the Logan plot. On the contrary, the latter noninvasive model has several distinct features compared with the original invasive and the former noninvasive models. First, this model is not a simple linear regression model but a multiple linear regression model. Therefore, a graphical plot with a straight-line fit is not provided; although the visualization of 3-dimensional hyper-plane fit is possible instead, its interpretation is not as straightforward as that of GA. In addition, this model includes the integration of $C_T(t)$ in contrast to the others. Nevertheless, it also avoids the requirement of a full dynamic scan like the others; this property of the original GP plot model is just transformed into the integration from t^* to t.

One drawback of these noninvasive methods is that the net accumulation of radioligand is acquired only in a relative or normalized form. Nevertheless, the former noninvasive model has found applications because of its history going back to 1985; the method has been frequently used in 6-[^{18}F]fluoro-*L*-dopa studies because of a good correlation between its own results and those from the invasive counterpart[92-95]. However, the latter method was

introduced in relatively recent years and thus has not been sufficiently investigated or used, and has been applied only to ROI data. Although the ROI results have shown good accuracy and precision, future parametric imaging may suffer from severe underestimation because $C_T(t)$ is used for independent variables.

Bi-graphical Analysis

Although GA generally provides robust parameter estimation by focusing on only two parameters, it may end up missing some information or exploiting only fragmentary information from given data. However, a combination of two methods or a dual application to different parts of the data may take full advantage of the data. In this sense, graphical methods to estimate V_T, which we went through in the previous subsections, can also be viewed as a bi-graphical technique when they are applied to target and reference regions separately to provide BP_{ND} computation.

RE-GP plots Recently, a bi-graphical analysis, named the RE-GP plot, has been proposed for the quantification of reversible tracer binding that may not be at the RE state during a PET scan because of slow binding kinetics as shown in Fig. 5 (right). Its model equation is given as follows,

$$\frac{\int_0^t C_T(s)ds}{C_T(t)} = V_{T,REGP}\frac{\int_0^t C_P(s)ds}{C_T(t)} + \beta_{REGP} \text{ for } t > t^*, \quad (27)$$

$$V_{T,REGP} = V_{T,RE} - \frac{\beta_{RE}}{\beta_{GP}}K_{in,GP}, \quad (28)$$

$$\beta_{REGP} = \frac{\beta_{RE}}{\beta_{GP}}, \quad (29)$$

where $V_{T,RE}$ and β_{RE}, (or $K_{in,GP}$ and β_{GP}) are the slope and intercept of the RE plot (or the GP plot) based on a plasma input function, respectively. Note that this RE-GP equation is the same as Equation (12) of the Logan plot except for the parameters. However, the parameters $V_{T,REGP}$ and β_{REGP} are estimated not by regression as in the Logan plot, but by arithmetic operations on the parameter estimates obtained by applying the RE plot and the GP plot separately. Thus, the RE-GP method requires the measurement of the plasma input function to estimate the parameters of the RE and GP plots.

The linearity period $t > t^*$ for the RE-GP method mainly follows that of the Logan plot[67]. It is better to use the t^* suitable for the Logan plot in each application of the RE plot and the GP plot rather than to determine and use the individual t^* for each plot; the t^* for each may be uncertain because of the slightly curved shape of the RE plot or high fluctuation in the GP plot as shown in Fig. 2.

The RE-GP plot maintains the properties of both plots, such as computational efficiency and statistical characteristics. As the RE plot and the GP plot have the same effectively noise-free independent variable in their model equation, accuracies of their target parameter estimates and thus those of the RE-GP method are not affected by noisy $C_T(t)$ in contrast to the Logan plot. However, the GP parameters are usually of high variance because of noisy $C_T(t)$ in the dependent variable (Figs. 3 and 6). Therefore, it is advantageous to apply a spatial smoothing filter to the GP parametric images before computing the parametric images of $V_{T,REGP}$ and β_{REGP}[67].

The original RE-GP can circumvent not only the bias issue in the Logan plot but also that of the RE plot (Fig. 3). As we introduced previously, the RE plot yields an underestimated V_T when sufficient time is not allowed for the tracer kinetics to reach the RE state (Fig. 3). The missing information, which the RE plot failed to capture because of the violation of the RE requirement, can be compensated for by the results from the GP plot (Fig. 3). In other words, the results of the RE plot describe the components achieving the RE state during the PET scan while those of the GP plot compensate for non-relative equilibrium components.

Ito plot Ito *et al.*[65] developed a form of bi-graphical analysis where the Yokoi plot[64] is applied to the early part of the data frames and the later part separately, and then the resulting parameters from the separate applications are combined to generate BP_{ND}, the parameter of interest; the Yokoi plot was originally proposed to estimate the cerebral blood flow (K_1) and the total distribution volume (V_T) only for tracers well described by the 1TCM, and was recently generalized into the Ito plot[65] for the neuroreceptor-radioligand binding studies where the 2TCM is involved. The Yokoi plot and thus the Ito plot rely upon the following linear relationship:

$$\frac{C_T(t)}{\int_0^t C_P(s)ds} = \beta_1\frac{\int_0^t C_T(s)ds}{\int_0^t C_P(s)ds} + \beta_2 \text{ for } t > t^* \text{ or } t \to 0. \quad (30)$$

Equation (30) yields a straight line through all data

frames (Fig. 7) when there is no specific binding in a target region (e.g., the Yokoi plot for 1TCM configuration tracers), and the slope (β_1), *y*-intercept (β_2), and *x*-intercept (β_2/β_1) of the regression line represent $-k_2$, K_1, and V_T (= V_{ND}), respectively. On the contrary, when applied to regions with specific binding (e.g., the Ito plot for 2TCM configuration tracers), Equation (30) generates a curve (Fig. 7) that reflects the dynamic effect of specific binding concentration on the measured tissue data. The fitted regression line can be characterized by $-k_2$ (slope), K_1 (y-intercept), and V_{ND} (*x*-intercept) for the early part of the data for $t \to 0$ in which $C_{ND}(t)$ dominates the measured tissue concentration $C_T(t)$. The line can be specified by $-k^*_{2a}$, $k^*_{2a}V_T$ and V_T (=V_{ND} + V_S), respectively, for late-part data ($t > t^*$) that can be approximately described with the 1TCM and its apparent rate constants $k^*_{2a}V_T$ (for influx) and k^*_{2a} (for efflux) after t^* (Ito *et al.* 2010[65, 67]); k^*_{2a} becomes k_{2a} (Fig. 1 and Equation (6)) when rapid equilibrium is established at $t^* \approx 0$ owing to relatively large k_3 and k_4. Care should be taken in V_{ND} estimation because the use of more data points increases not only the reliability of estimation but also the bias due to the violation of $C_T(t) \approx C_{ND}(t)$ for $t \to 0$[96].

Based upon the plot characteristics that vary according to the model configuration, the Ito plot model (Equation (30)) can be useful for graphically distinguishing whether a target region is devoid of specific binding or not[65]. Furthermore, the Ito plot can be used to compute BP_{ND} using the resulting V_{ND} and V_T estimates. The major distinction between this and other reference region methods is that *a priori* knowledge of the reference region is not required. These features may be obtained with the Logan plot because the Ito plot and the Logan plot are based on the same linear relationship except for the different arrangement of parameters and variables (thereby, different noise characteristics). Note that the Yokoi and Ito plots are both GA techniques for V_T estimation, even though we introduce them here as bi-graphical analysis methods for BP_{ND} generation.

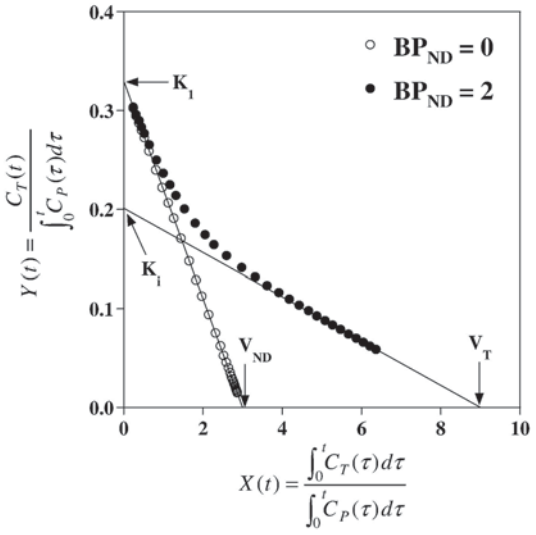

Fig. 7. An example of Ito plot analysis. The *y*- and *x*-intercepts of the regression line represent K_1 and V_{ND}, respectively, for early data frames, whereas $K_i = k^*_{2a}V_T$ and V_T for the late part of the data (after the equilibrium time) (reprinted from Ito *et al.* Neuroimage 2010[65] with permission). Open (or filled) circles display examples of applications for one- (or two-) tissue compartment model data.

On the other hand, the main drawback of the Yokoi and Ito plots is that the precision of estimates is usually low because of noise effects[65, 69, 96], particularly at the voxel-level, for several reasons: (1) the dependent variable includes $C_T(t)$, the major source of noise in kinetic modeling, as its numerator; (2) the estimation of V_{ND} involves early time frames, usually with a very low SNR[8]; and (3) the parameters of interest, V_T and V_{ND}, are computed by dividing the *y*-intercept by the slope. Therefore, as shown in Figure 8, the de-noising of dynamic images is essential to improve the SNR of parametric images[8, 96].

Summary

PET research has greatly contributed to advance our understanding of the brain in health and disease[4, 97-102]; quantitative neuroreceptor mapping with kinetic modeling has played a key role in such contributions by offering accurate visualization and voxel-wise analysis of the distribution and activity of various neuroreceptors that are the most influential structures in the brain.

In this article, we have presented an overview of GA-based parametric image generation from dynamic neuroreceptor PET data. Although parametric imaging may cover broad concepts, including the voxel-wise measurement of standard uptake values from a single static image, or other standard kinetic parameters such as peak concentration from dynamic data[5, 8, 31], throughout the paper, it refers to a voxel-wise application of specific mathematical modeling approaches to analyze

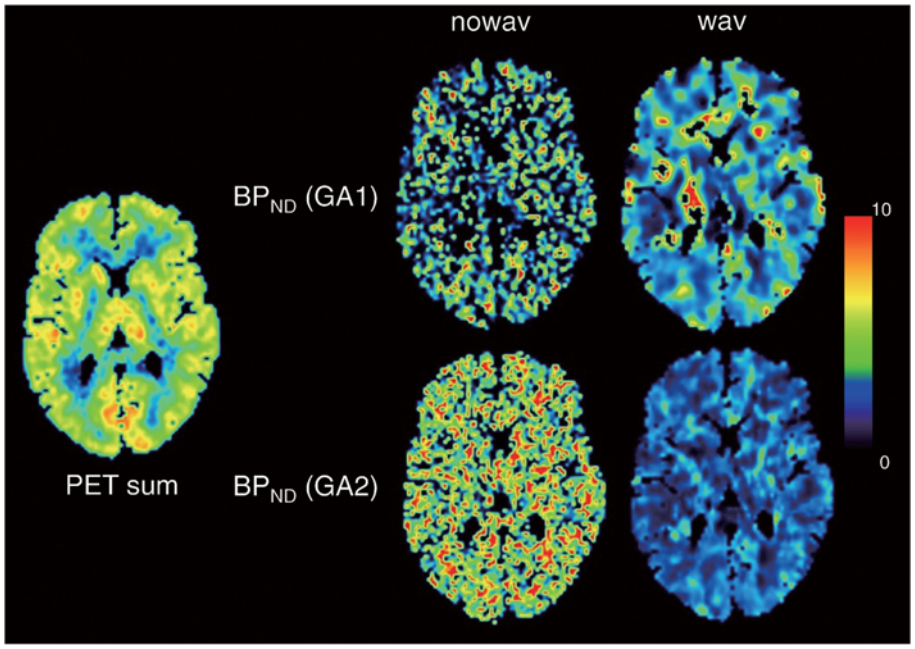

Fig. 8. *BP*$_{ND}$ images obtained by the Ito plot (upper, GA1) and the Logan plot (lower, GA2) from dynamic PET with [^{18}F]FEDAA1106, a radioligand for translocator protein imaging, before wavelet de-noising (nowav) and after wavelet de-noising (wav) (reprinted from Ikoma *et al.* Neuroimage 2013[96] with permission).

reconstructed dynamic PET images. In GA methods, a simple linear model with only two parameters is used to fit only the later portion of the measured data. Thanks to the linearization and simplification of the underlying model, GA methods achieve very desirable parametric imaging that is independent of any compartmental model configuration, robust to noise, and computationally efficient. However, both the linearization and simplification depend on several assumptions that are commonly hard to satisfy simultaneously. Therefore, the recent advances in GA approaches have been mainly based on a reduction of specific assumptions or replacement with new ones.

Recently, parametric imaging techniques have shown two major trends: a conventional pipeline of analyzing the reconstructed dynamic data and a direct reconstruction of parametric images from coincidence count data[17, 20]. Although the direct reconstruction technique is considered as the ultimate path for parametric image generation because of its potential advantages in high-resolution PET[17], this field was inactive until recently despite its early emergence and has several challenges to address, such as high algorithmic complexity[20]. Therefore, we believe that the indirect parametric imaging methods, especially the GA techniques we have considered, are still invaluable and furthermore will play a leading role in achieving the ultimate goal. We refer readers interested in direct parametric imaging to a comprehensive review by Wang and Qi[20], since it is beyond the scope of this paper.

ACKNOWLEDGMENTS

This review was supported by a grant from the Korea Healthcare Technology R&D Project, Ministry of Health & Welfare, Republic of Korea (HI13C01630200) and by the Industrial Strategic Technology Development Program (10030030) funded by the Ministry of Trade, Industry & Energy, Korea.

Received date: 2014-06-08; Accepted date: 2014-08-15

REFERENCES

[1] Ichise M, Meyer JH, Yonekura Y. An introduction to PET and SPECT neuroreceptor quantification models. J Nucl Med 2001, 42: 755–763.

[2] Meyer JH, Ichise M. Modeling of receptor ligand data in PET and SPECT imaging: A review of major approaches. J

Neuroimaging 2001, 11: 30–39.

[3] Watabe H, Ikoma Y, Kimura Y, Naganawa M, Shidahara M. PET kinetic analysis—compartmental model. Ann Nucl Med 2006, 20: 583–588.

[4] Zaidi H, Shidahara M. Neuroreceptor imaging. In: Choi IY and Gruetter R (Eds.). Neural Metabolism *In Vivo*. New York, USA: Springer, 2012: 305–329.

[5] Lee JS, Lee DS. Tracer kinetic analysis for PET and SPECT. Medical Imaging: Technology and Applications 2013.

[6] Mintun MA, Raichle ME, Kilbourn MR, Wooten GF, Welch MJ. A quantitative model for the *in vivo* assessment of drug binding sites with positron emission tomography. Ann Neurol 1984, 15: 217–227.

[7] Carson RE. Tracer kinetic modeling in PET. In: Bailey DL, Townsend DW, Valk PE, Maisey MN (Eds). Positron Emission Tomography. London, Springer, 2005: 127–159.

[8] Feng DD. Biomedical Information Technology. Academic Press, 2008.

[9] Cherry SR, Sorenson JA, Phelps ME. Physics in Nuclear Medicine. Elsevier Health Sciences, 2012.

[10] Koeppe R, Holthoff V, Frey K, Kilbourn M, Kuhl D. Compartmental analysis of [^{11}C]flumazenil kinetics for the estimation of ligand transport rate and receptor distribution using positron emission tomography. J Cereb Blood Flow Metab 1991, 11: 735–744.

[11] Kazumata K, Dhawan V, Chaly T, Antonini A, Margouleff C, Belakhlef A*, et al.* Dopamine transporter imaging with fluorine-18-FPCIT and PET. J Nucl Med 1998, 39: 1521–1530.

[12] Chen M-K, Lee J-S, McGlothan JL, Furukawa E, Adams RJ, Alexander M*, et al.* Acute manganese administration alters dopamine transporter levels in the non-human primate striatum. Neurotoxicology 2006, 27: 229–236.

[13] Lim K, Kwon J, Jang I, Jeong J, Lee J, Kim H*, et al.* Modeling of brain D_2 receptor occupancy-plasma concentration relationships with a novel antipsychotic, YKP1358, using serial PET scans in healthy volunteers. Clin Pharmacol Ther 2007, 81: 252–258.

[14] Weerts EM, Kim YK, Wand GS, Dannals RF, Lee JS, Frost JJ*, et al.* Differences in *δ*-and *μ*-opioid receptor blockade measured by positron emission tomography in naltrexone-treated recently abstinent alcohol-dependent subjects. Neuropsychopharmacology 2008, 33: 653–665.

[15] Kim JW, Lee JS, Kim SJ, Hoigebazar L, Shin KH, Yu KS*, et al.* Compartmental modeling and simplified quantification of [^{11}C]sertraline distribution in human brain. Arch Pharm Res 2012, 35: 1591–1597.

[16] Lee JY, Seo SH, Kim YK, Yoo HB, Kim YE, Song IC*, et al.* Extrastriatal dopaminergic changes in Parkinson's disease patients with impulse control disorders. J Neurol Neurosurg Psychiatry 2014, 85: 23–30.

[17] Carson RE. Tracer kinetic parametric imaging in PET. In: 2004 2nd IEEE International Symposium on Biomedical Imaging: Nano to Macro. 2004: 611–615.

[18] Lee JS, Lee DS, Ahn JY, Yeo JS, Cheon GJ, Kim S-K*, et al.* Generation of parametric image of regional myocardial blood flow using $H_2{}^{15}O$ dynamic PET and a linear least-squares method. J Nucl Med 2005, 46: 1687–1695.

[19] Cselényi Z, Olsson H, Halldin C, Gulyás B, Farde L. A comparison of recent parametric neuroreceptor mapping approaches based on measurements with the high affinity PET radioligands [^{11}C]FLB 457 and [^{11}C]WAY 100635. Neuroimage 2006, 32: 1690–1708.

[20] Wang G, Qi J. Direct estimation of kinetic parametric images for dynamic PET. Theranostics 2013, 3: 802–815.

[21] Gunn RN, Lammertsma AA, Hume SP, Cunningham VJ. Parametric imaging of ligand-receptor binding in PET using a simplified reference region model. Neuroimage 1997, 6: 279–287.

[22] Kim SJ, Lee JS, Kim YK, Frost J, Wand G, McCaul ME*, et al.* Multiple linear analysis methods for the quantification of irreversibly binding radiotracers. J Cereb Blood Flow Metab 2008, 28: 1965–1977.

[23] Wienhard K, Schmand M, Casey ME, Baker K, Bao J, Eriksson L*, et al.* The ECAT HRRT: performance and first clinical application of the new high resolution research tomograph. IEEE Transactions on Nuclear Science 2002, 49: 104–110.

[24] Zhou Y, Huang SC, Bergsneider M, Wong DF. Improved parametric image generation using spatial-temporal analysis of dynamic PET studies. Neuroimage 2002, 15: 697–707.

[25] Alpert NM, Yuan F. A general method of Bayesian estimation for parametric imaging of the brain. Neuroimage 2009, 45: 1183–1189.

[26] Dean Fang Y-H, El Fakhri G, Becker JA, Alpert NM. Parametric imaging with Bayesian priors: A validation study with ^{11}C-Altropane PET. Neuroimage 2012, 61: 131–138.

[27] Kamasak M. Effects of spatial regularization on kinetic parameter estimation for dynamic PET. Biomed Signal Process Control 2014, 9: 6–13.

[28] Innis RB, Cunningham VJ, Delforge J, Fujita M, Gjedde A, Gunn RN*, et al.* Consensus nomenclature for *in vivo* imaging of reversibly binding radioligands. J Cereb Blood Flow Metab 2007, 27: 1533–1539.

[29] Gunn RN, Gunn SR, Cunningham VJ. Positron emission tomography compartmental models. J Cereb Blood Flow Metab 2001, 21: 635–652.

[30] Morris ED, Endres CJ, Schmidt KC, Christian BT, Muzic RFJ, Fisher RE. Kinetic modeling in positron emission tomography. In: Wernick MN, Aarsvold JN. Emission Tomography: The

Fundamentals of PET and SPECT. Elsevier, 2004: 499–540.
[31] Bentourkia Mh, Zaidi H. Tracer kinetic modeling in PET. PET Clinics 2007, 2: 267–277.
[32] Huang S-C, Barrio JR, Phelps ME. Neuroreceptor assay with positron emission tomography: equilibrium versus dynamic approaches. J Cereb Blood Flow Metab 1986, 6: 515–521.
[33] Lammertsma AA, Hume SP. Simplified reference tissue model for PET receptor studies. Neuroimage 1996, 4: 153–158.
[34] Phelps M, Huang S, Hoffman E, Selin C, Sokoloff L, Kuhl D. Tomographic measurement of local cerebral glucose metabolic rate in humans with (F–18) 2-fluoro-2-deoxy-D-glucose: validation of method. Ann Neurol 1979, 6: 371–388.
[35] Huang S-C, Phelps ME, Hoffman EJ, Sideris K, Selin CJ, Kuhl DE. Noninvasive determination of local cerebral metabolic rate of glucose in man. Am J Physiol 1980, 238: E69–E82.
[36] Ogden RT. Estimation of kinetic parameters in graphical analysis of PET imaging data. Stat Med 2003, 22: 3557–3568.
[37] Wu YG. Noninvasive quantification of local cerebral metabolic rate of glucose for clinical application using positron emission tomography and ^{18}F-fluoro-2-deoxy-D-glucose. J Cereb Blood Flow Metab 2008, 28: 242–250.
[38] Zheng X, Wen L, Yu SJ, Huang SC, Feng DD. A study of non-invasive Patlak quantification for whole-body dynamic FDG-PET studies of mice. Biomed Signal Process Control 2012, 7: 438–446.
[39] Chen K, Bandy D, Reiman E, Huang SC, Lawson M, Feng D*, et al.* Noninvasive quantification of the cerebral metabolic rate for glucose using positron emission tomography, ^{18}F-fluoro-2-deoxyglucose, the Patlak method, and an image-derived input function. J Cereb Blood Flow Metab 1998, 18: 716–723.
[40] Kim SJ, Lee JS, Im KC, Kim SY, Park SA, Lee SJ*, et al.* Kinetic modeling of 3′-deoxy-3′-^{18}F-fluorothymidine for quantitative cell proliferation imaging in subcutaneous tumor models in mice. J Nucl Med 2008, 49: 2057–2066.
[41] Kim JH, Kim YH, Kim YJ, Yang BY, Jeong JM, Youn H*, et al.* Quantitative positron emission tomography imaging of angiogenesis in rats with forelimb ischemia using ^{68}Ga-NOTA-c(RGDyK). Angiogenesis 2013, 16: 837–846.
[42] Feng D, Huang SC, Wang X. Models for computer simulation studies of input functions for tracer kinetic modeling with positron emission tomography. Int J Biomed Comput 1993, 32: 95–110.
[43] Phillips RL, Chen CY, Wong DF, London ED. An improved method to calculate cerebral metabolic rates of glucose using PET. J Nucl Med 1995, 36: 1668–1679.
[44] Takikawa S, Dhawan V, Spetsieris P, Robeson W, Chaly T, Dahl R*, et al.* Noninvasive quantitative fluorodeoxyglucose PET studies with an estimated input function derived from a population-based arterial blood curve. Radiology 1993, 188: 131–136.
[45] Cunningham VJ, Hume SP, Price GR, Ahier RG, Cremer JE, Jones A. Compartmental analysis of diprenorphine binding to opiate receptors in the rat *in vivo* and its comparison with equilibrium data *in vitro*. J Cereb Blood Flow Metab 1991, 11: 1–9.
[46] Hume SP, Myers R, Bloomfield PM, Opacka-Juffry J, Cremer JE, Ahier RG*, et al.* Quantitation of Carbon-11-labeled raclopride in rat striatum using positron emission tomography. Synapse 1992, 12: 47–54.
[47] Lammertsma A, Bench C, Hume S, Osman S, Gunn K, Brooks D*, et al.* Comparison of methods for analysis of clinical [^{11}C]raclopride studies. J Cereb Blood Flow Metab 1996, 16: 42–52.
[48] Watabe H, Carson R, Iida H. The reference tissue model: Three compartments for the reference region. Neuroimage 2000, 11: S12.
[49] Feng D, Wong KP, Wu CM, Siu WC. A technique for extracting physiological parameters and the required input function simultaneously from PET image measurements: Theory and simulation study. IEEE Trans Inf Technol Biomed 1997, 1: 243–254.
[50] Watabe H, Channing MA, Riddell C, Jousse F, Libutti SK, Carrasquillo JA*, et al.* Noninvasive estimation of the aorta input function for measurement of tumor blood flow with [^{15}O] water. IEEE Trans Med Imaging 2001, 20: 164–174.
[51] Wu HM, Hoh CK, Choi Y, Schelbert HR, Hawkins RA, Phelps ME*, et al.* Factor analysis for extraction of blood time-activity curves in dynamic FDG-PET studies. J Nucl Med 1995, 36: 1714–1722.
[52] Lee JS, Lee DS, Ahn JY, Cheon GJ, Kim SK, Yeo JS*, et al.* Blind separation of cardiac components and extraction of input function from $H_2{}^{15}O$ dynamic myocardial PET using independent component analysis. J Nucl Med 2001, 42: 938–943.
[53] Ahn JY, Lee DS, Lee JS, Kim SK, Cheon GJ, Yeo JS*, et al.* Quantification of regional myocardial blood flow using dynamic $H_2{}^{15}O$ PET and factor analysis. J Nucl Med 2001, 42: 782–787.
[54] Naganawa M, Kimura Y, Ishii K, Oda K, Ishiwata K, Matani A. Extraction of a plasma time-activity curve from dynamic brain PET images based on independent component analysis. IEEE Trans Biomed Eng 2005, 52: 201–210.
[55] Parker BJ, Feng DD. Graph-based Mumford-Shah segmentation of dynamic PET with application to input function estimation. IEEE Trans Nucl Sci 2005, 52: 79–89.
[56] Zanderigo F, Ogden RT, Parsey RV. Reference region

approaches in PET: a comparative study on multiple radioligands. J Cereb Blood Flow Metab 2013, 33: 888–897.

[57] Logan J, Fowler JS, Volkow ND, Wang GJ, Ding YS, Alexoff DL. Distribution volume ratios without blood sampling from graphical analysis of PET data. J Cereb Blood Flow Metab 1996, 16: 834–840.

[58] Wong DF, Wagner HN, Dannals RF, Links JM, Frost JJ, Ravert HT*, et al.* Effects of age on dopamine and serotonin receptors measured by positron tomography in the living human brain. Science 1984, 226: 1393–1396.

[59] Beck JV, Arnold KJ. Parameter Estimation in Engineering and Science. New York: John Wiley & Sons, 1977.

[60] Gjedde A. High- and low-affinity transport of D-glucose from blood to brain. J Neurochem 1981, 36: 1463–1471.

[61] Patlak CS, Blasberg RG, Fenstermacher JD. Graphical evaluation of blood-to-brain transfer constants from multiple-time uptake data. J Cereb Blood Flow Metab 1983, 3: 1–7.

[62] Patlak CS, Blasberg RG. Graphical evaluation of blood-to-brain transfer constants from multiple-time uptake data. Generalizations. J Cereb Blood Flow Metab 1985, 5: 584–590.

[63] Logan J, Fowler JS, Volkow ND, Wolf AP, Dewey SL, Schlyer DJ*, et al.* Graphical analysis of reversible radioligand binding from time-activity measurements applied to [*N*-^{11}C-methyl]-(−)-cocaine PET studies in human subjects. J Cereb Blood Flow Metab 1990, 10: 740–747.

[64] Yokoi T, Iida H, Itoh H, Kanno I. A new graphic plot analysis for cerebral blood flow and partition coefficient with iodine-123-iodoamphetamine and dynamic SPECT validation studies using oxygen-15-water and PET. J Nucl Med 1993, 34: 498–505.

[65] Ito H, Yokoi T, Ikoma Y, Shidahara M, Seki C, Naganawa M*, et al.* A new graphic plot analysis for determination of neuroreceptor binding in positron emission tomography studies. Neuroimage 2010, 49: 578–586.

[66] Zhou Y, Ye W, Brašić JR, Crabb AH, Hilton J, Wong DF. A consistent and efficient graphical analysis method to improve the quantification of reversible tracer binding in radioligand receptor dynamic PET studies. Neuroimage 2009, 44: 661–670.

[67] Zhou Y, Ye W, Brašić JR, Wong DF. Multi-graphical analysis of dynamic PET. Neuroimage 2010, 49: 2947–2957.

[68] Logan J. A review of graphical methods for tracer studies and strategies to reduce bias. Nucl Med Biol 2003, 30: 833–844.

[69] Logan J, Alexoff D, Fowler JS. The use of alternative forms of graphical analysis to balance bias and precision in PET images. J Cereb Blood Flow Metab 2011, 31: 535–546.

[70] Schmidt KC, Turkheimer FE. Kinetic modeling in positron emission tomography. quarterly J Nucl Med 2002, 46: 70–85.

[71] Ichise M, Ballinger JR, Golan H, Vines D, Luong A, Tsai S*, et al.* Noninvasive quantification of dopamine D_2 receptors with iodine-123-IBF SPECT. J Nucl Med 1996, 37: 513–520.

[72] Carson RE. PET parameter estimation using linear integration methods: Bias and variability considerations. In: Uemura K, Lassen NA, Jones Y, Kanno I (Eds). Quantification of Brain Function: Tracer Kinetics and Image Analysis in Brain PET. Amsterdam: Elsevier Science Publishers, 1993.

[73] Abi-Dargham A, Martinez D, Mawlawi O, Simpson N, Hwang DR, Slifstein M*, et al.* Measurement of striatal and extrastriatal dopamine D_1 receptor binding potential With [^{11}C] NNC 112 in humans: validation and reproducibility. J Cereb Blood Flow Metab 2000, 20: 225–243.

[74] Slifstein M, Laruelle M. Effects of statistical noise on graphic analysis of PET neuroreceptor studies. J Nucl Med 2000, 41: 2083–2088.

[75] Kimura Y, Naganawa M, Shidahara M, Ikoma Y, Watabe H. PET kinetic analysis—Pitfalls and a solution for the Logan plot. Ann Nucl Med 2007, 21: 1–8.

[76] Logan J, Fowler JS, Volkow ND, Ding YS, Wang GJ, Alexoff DL. A strategy for removing the bias in the graphical analysis method. J Cereb Blood Flow Metab 2001, 21: 307–320.

[77] Logan J, Fowler JS, Ding YS, Franceschi D, Wang GJ, Volkow ND*, et al.* Strategy for the formation of parametric images under conditions of low injected radioactivity applied to PET studies with the irreversible monoamine oxidase A tracers [^{11}C]Clorgyline and Deuterium-substituted [^{11}C] Clorgyline. J Cereb Blood Flow Metab 2002, 22: 1367–1376.

[78] Varga J, Szabo Z. Modified regression model for the Logan plot. J Cereb Blood Flow Metab 2002, 22: 240–244.

[79] Joshi A, Fessler JA, Koeppe RA. Improving PET receptor binding estimates from Logan plots using principal component analysis. J Cereb Blood Flow Metab 2008, 28: 852–865.

[80] Cselényi Z, Olsson H, Farde L, Gulyás B. Wavelet-aided parametric mapping of cerebral dopamine D_2 receptors using the high affinity PET radioligand [^{11}C]FLB 457. Neuroimage 2002, 17: 47–60.

[81] Shidahara M, Seki C, Naganawa M, Sakata M, Ishikawa M, Ito H*, et al.* Improvement of likelihood estimation in Logan graphical analysis using maximum a posteriori for neuroreceptor PET imaging. Ann Nucl Med 2009, 23: 163–171.

[82] Feng D, Huang SC, Wang Z, Ho D. An unbiased parametric imaging algorithm for nonuniformly sampled biomedical system parameter estimation. IEEE Trans Med Imaging 1996, 15: 512–518.

[83] Kimura Y, Hsu H, Toyama H, Senda M, Alpert NM. Improved signal-to-noise ratio in parametric images by cluster analysis. Neuroimage 1999, 9: 554–561.

[84] Van Huffel S, Vandewalle J. The total least squares problem:

computational aspects and analysis. Frontiers Appl Math SIAM, Philadelphia, 1991.

[85] Ichise M, Toyama H, Innis RB, Carson RE. Strategies to improve neuroreceptor parameter estimation by linear regression analysis. J Cereb Blood Flow Metab 2002, 22: 1271–1281.

[86] Parsey RV, Ogden RT, Mann JJ. Determination of volume of distribution using likelihood estimation in graphical analysis: elimination of estimation bias. J Cereb Blood Flow Metab 2003, 23: 1471–1478.

[87] Young PC. An instrumental variable method for real-time identification of a noisy process. Automatica 1970, 6: 271–287.

[88] Stoica P, Soderstrom T. Optimal instrumental variable estimation and approximate implementations. IEEE Trans Automat Contr 1983, 28: 757–772.

[89] Stock JH, Watson MW. Introduction to Econometrics. Addison Wesley, 2003.

[90] Van Huffel S, Vandewalle J. Comparison of total least squares and instrumental variable methods for parameter estimation of transfer function models. Int J Contr 1989, 50: 1039–1056.

[91] Minchin P. Analysis of tracer profiles with applications to phloem transport. J Exp Bot 1978, 29: 1441–1450.

[92] Brooks D, Salmon E, Mathias C, Quinn N, Leenders K, Bannister R*, et al*. The relationship between locomotor disability, autonomic dysfunction, and the integrity of the striatal dopaminergic system in patients with multiple system atrophy, pure autonomic failure, and Parkinson's disease, studied with PET. Brain 1990, 113: 1539–1552.

[93] Howes OD, Montgomery AJ, Asselin M, Murray RM, Grasby PM, McGUIRE PK. Molecular imaging studies of the striatal dopaminergic system in psychosis and predictions for the prodromal phase of psychosis. Br J Psychiatry 2007, 191: s13–s18.

[94] Howes OD, Montgomery AJ, Asselin MC, Murray RM, Valli I, Tabraham P*, et al.* Elevated striatal dopamine function linked to prodromal signs of schizophrenia. Arch Gen Psychiatry 2009, 66: 13–20.

[95] Kumakura Y, Cumming P. PET studies of cerebral levodopa metabolism: a review of clinical findings and modeling approaches. Neuroscientist 2009, 15: 635–650.

[96] Ikoma Y, Takano A, Varrone A, Halldin C. Graphic plot analysis for estimating binding potential of translocator protein (TSPO) in positron emission tomography studies with [^{18}F]FEDAA1106. Neuroimage 2013, 69: 78–86.

[97] Heiss WD, Herholz K. Brain receptor imaging. J Nucl Med 2006, 47: 302–312.

[98] Woo S, Kim S, Zhou J, Kim E, Seo JM, Park J*, et al.* Imaging of activated cortical areas after light and electrical stimulation of the rabbit retina: F-18 FDG PET-guided brain mapping. Biomed Eng Lett 2012, 2: 111–117.

[99] Jin S, Oh M, Oh S, Oh J, Lee S, Chung S*, et al.* Differential diagnosis of Parkinsonism using dual-phase F-18 FP-CIT PET imaging. Nucl Med Mol Imaging 2013, 47: 44–51.

[100] Park E, Hwang Y, Lee CN, Kim S, Oh S, Kim Y*, et al*. Differential diagnosis of patients with inconclusive Parkinsonian features using [18F]FP-CIT PET/CT. Nucl Med Mol Imaging 2014, 48: 106–113.

[101] Lee SH, Park H. Parametric response mapping of longitudinal PET scans and their use in detecting changes in Alzheimer's diseases. Biomed Eng Lett 2014, 4: 73–79.

[102] Brust P, Hoff J, Steinbach J. Development of ^{18}F-labeled radiotracers for neuroreceptor imaging with positron emission tomography. Neurosci Bull 2014. Doi: 10.1007/s12264-014-1460-6.